Magnetotactic bacteria accumulate a large pool of iron distinct from their magnetite crystals

Matthieu Amor[1]*, Alejandro Ceballos[2], Juan Wan[1], Christian P. Simon[3], Allegra T. Aron[4,5,6], Christopher J. Chang[4,7], Frances Hellman[2,3,8], Arash Komeili[1,7]

[1] Department of Plant and Microbial Biology, University of California, Berkeley, CA 94720-3102

[2] Department of Materials Science and Engineering, University of California, Berkeley, California 94720

[3] Department of Physics, University of California, Berkeley, California 94720

[4] Department of Chemistry, University of California, Berkeley, CA 94720

[5] Skaggs School of Pharmacy and Pharmaceutical Sciences, University of California, San Diego, La Jolla, CA 92093, USA

[6] Collaborative Mass Spectrometry Innovation Center, University of California, San Diego, La Jolla, CA 92093, USA

[7] Department of Molecular and Cell Biology, University of California, Berkeley, CA 94720-3200

[8] Materials Sciences Division, Lawrence Berkeley National Laboratory, Berkeley, California 94720

* Present address: CNRS, CEA, Aix-Marseille Université, UMR7265 Biosciences and Biotechnologies Institute of Aix-Marseille, Saint Paul lez Durance, France.

Corresponding authors: matthieu.amor@cea.fr (MA); komeili@berkeley.edu (AK)

Abstract

Magnetotactic bacteria (MTB) are ubiquitous aquatic microorganisms that form intracellular nanoparticles of magnetite (Fe_3O_4) or greigite (Fe_3S_4) in a genetically controlled manner. Magnetite and greigite synthesis requires MTB to transport a large amount of iron from the environment which is subsequently concentrated in organelles called magnetosomes for crystal precipitation and maturation. X-ray absorption analysis of MTB suggests that the intracellular iron is mainly contained within the crystals, thus preventing potential toxic effects of free iron. In contrast, recent mass spectrometry studies suggest that MTB may contain a large amount of iron that is not precipitated in crystals. Here, we attempt to resolve these descrepancies by performing chemical and magnetic assays to quantify the different iron pools in the magnetite-forming strain *Magnetospirillum magneticum* AMB-1 cultivated at varying iron concentrations. AMB-1 mutants showing defects in crystal precipitation were also characterized following the same approach. All results show that magnetite represents at most 30 % of the total intracellular iron under our experimental conditions. We further examined the iron speciation and subcellular localization in AMB-1 using the fluorescent indicator FIP-1 that is designed for detection of labile Fe(II). Staining with this probe suggests that unmineralized reduced iron is found in the cytoplasm and associated with magnetosomes. Our results demonstrate that, under our experimental conditions, AMB-1 is able to accumulate a large pool of iron distinct from magnetite. Finally, we discuss the biochemical and geochemical implications of these results.

Importance

Magnetotactic bacteria (MTB) are a group of microorganisms producing iron-based intracellular magnetic crystals. They represent a model system for studying iron homeostasis and biomineralization in bacteria. MTB contain an important mass of iron, about 10 to 100 higher than other bacterial model such as *Escherichia coli*, suggesting efficient iron uptake and storage systems. Accordingly, MTB have been proposed to significantly impact the iron biogeochemical cycle in sequestering a large amount of soluble iron into crystals. Recently, several studies proposed that MTB could also accumulate iron in a reservoir distinct from their crystals. Here, we present a chemical and magnetic methodology for quantifying the fraction of the total cellular iron contained in the magnetic crystals of the magnetotactic strain *Magnetospirillum magneticum* AMB-1. Comparison of the mass of iron contained in the different cellular pools showed that most of the bacterial iron is not contained in AMB-1 crystals. We then adapted protocols for the fluorescent detection of Fe(II) in bacteria, and showed that iron could be detected outside of crystals using fluorescence assays. This work suggests a more complex picture for iron homeostasis in MTB than previously thought. Because iron speciation controls its solubility, our results also provide important insights into the geochemical impact of MTB. A large pool of unmineralized iron in MTB could be more easily released in the environment than magnetite, thus limiting iron sequestration into MTB crystals.

Introduction

Many living organisms transform inorganic molecules into crystalline structures in a process called biomineralization. Magnetotactic bacteria (MTB) represent an elegant example of such organisms. They incorporate dissolved iron from their environment and precipitate it as magnetite [$Fe(II)Fe(III)_2O_4$] or greigite [$Fe(II)Fe(III)_2S_4$] nanoparticles in organelles called magnetosomes (Uebe and Schüler, 2016). MTB are ubiquitous gram-negative microorganisms in aquatic environments. They inhabit the oxic/anoxic transition zones in the water column or sediments where they thrive (Kopp and Kirschvink, 2008). In MTB, magnetosomes are aligned as chains inside the cell, and provide the bacteria with a permanent magnetic dipole presumably for navigation purposes (Uebe and Schüler, 2016).

Tremendous work has been carried out to determine the biological and chemical reactions leading to magnetite synthesis in MTB (McCausland and Komeili, 2020). In the two best-studied, magnetite-forming strains *Magnetospirillum magneticum* AMB-1 and *Magnetospirillum gryphiswaldense* MSR-1, magnetosome formation is a genetically-controlled process where: (*i*) magnetosome vesicles are formed from invagination of the inner cell membrane, (*ii*) empty magnetosome vesicles are aligned as a chain inside the cell, (*iii*) iron is transported and concentrated into magnetosome for initiation of biomineralization, and (*iv*) crystal size and shape are precisely controlled in a species-specific manner. A set of ~30 genes, located in a distinct portion of the genome called the magnetosome island (MAI), is required and sufficient for the step-wise formation of magnetosomes (Murat *et al*, 2010). Recently, iron isotope studies have provided an integrative model for iron uptake and precipitation as magnetite in the magnetotactic strain AMB-1 (Amor *et al*, 2016, 2018). This model assumes that dissolved Fe(II) or Fe(III) species are incorporated into AMB-1 and stored in the cytoplasm and/or periplasm as Fe(III). This Fe(III) pool is then partially reduced into Fe(II) for trafficking to magnetosomes, and oxidized for precipitation as magnetite

(Amor *et al*, 2018). Direct mass spectrometry measurements of iron content and iron isotope composition in AMB-1 cells devoid of magnetosomes suggests that a large pool of iron, which could represent at least 50% of the total cellular iron, accumulate in reservoir(s) distinct from magnetite (Amor *et al*, 2016, 2018). The above-mentioned high-resolution mass spectrometry measurements of iron showed discrepancy with previous X-ray absorption analyses performed on both AMB-1 and MSR-1 strains, in which magnetite was the sole iron species detected at the end of the biomineralization process (Baumgartner *et al*, 2013; Fdez-Gubieda *et al*, 2013).

In the present work, we address the discrepancy between the mass spectrometry and X-ray absorption experiments by determining the distribution of iron in AMB-1 cells. We grew AMB-1 with different iron concentrations, and measured the mass of iron taken up by the bacteria using chemical assays. Cells were then recovered and the mass of iron contained in magnetite was quantified from magnetic characterizations. From these experimental results, we found that magnetite represents ~25 to ~30% of the bulk cellular iron. Additional cultures of AMB-1 were grown to determine the total mass of iron contained in magnetite at the scale of a bacterial population. Simultaneous cell counting allowed us to estimate the mean mass of magnetite per cell. Comparison of these results with published single-cell quantification of bulk iron in AMB-1 supported mass balance estimations. Finally, we used a fluorescent reporter of iron to show that at least part of the non-crystalline iron is present as Fe(II) species within bacterial cells. To further investigate the link between magnetite formation and iron incorporation, mutant AMB-1 strains (Δ*mamP* and Δ*mamT* strains lacking the protein MamP and MamT, respectively) showing biomineralization defects were also analyzed following the same approaches (Fig. 1). Bacterial cultures of all strains were carried out in triplicates.

All data support the presence a large pool of iron, at least partially reduced, distinct from magnetite in AMB-1 under our experimental conditions. These results raise important

biochemical (*i.e.* iron homeostasis in MTB) and geochemical (*i.e.* impact of MTB on the iron biogeochemical cycle) questions that we address in the discussion of this article.

Results

Iron depletion and speciation in AMB-1 cultures

We first cultivated wild-type AMB-1 (Fig. 1) for three days at two iron concentrations (30 and 150 μM). Sterile media containing no bacteria were also prepared and used as a control condition. The iron concentration and oxidation state were monitored in AMB-1 cultures and sterile media using the ferrozine assay (see materials and methods). Iron concentration and oxidation state in the filtered sterile media remained constant over the three days of incubation, showing that all iron in the growth media can be analyzed by the ferrozine assay (Table 1; Fig. 2). Therefore, the decrease in iron concentration in the growth media is not due to precipitation of small iron phases excluded during filtration and can be attributed to iron uptake by AMB-1. Initial and final Fe(II), total iron concentration and pH in wild-type AMB-1 growth media, as well as final optical densities (OD_{400nm}), are given in Table 2. Most of the bacterial iron uptake, normalized to biomass, occurred between one and two days of culture (Fig. 2): iron depletion was 0.10 ± 0.04 and 0.95 ± 0.21 mg per unit of optical density after 26 hours of culture for an initial iron concentration of 30 and 150 μM, respectively; and 0.37 ± 0.03 and 1.05 ± 0.15 mg per unit of optical density after 46 hours of culture for an initial iron concentration of 30 and 150 μM, respectively (Fig. 3A). For an initial concentration of 30 μM, no further iron depletion occurred after 46 h of culture. In contrast, the mass of iron depleted from the growth medium decreased to 0.69 ± 0.18 mg per unit of optical density in cultures provided with 150 μM of iron. Iron speciation was also modified over bacterial growth. 40 and 17% of the initial Fe(III) added to the growth media containing 30 and 150 μM of iron, respectively, became immediately reduced after inoculation (Fig. 4). Remaining Fe(III) was

then progressively reduced until complete reduction, which happened after 46 and 69 hours of culture for an initial iron concentration of 30 and 150 µM, respectively. Finally, the growth medium pH showed a similar increase between the two iron conditions, with final values of ~7.5 (Table 2).

Iron uptake by the two mutant Δ*mamP* and Δ*mamT* strains was then measured following the same experimental procedure. Because mutant strains produce less magnetite than wild-type AMB-1, as shown by the electron microscope observations (Fig. 1), we cultivated them with iron at 150 µM to measure iron uptake more accurately. The highest iron uptake by wild-type AMB-1 was observed at ~45 h of culture (see results). Accordingly, Δ*mamP* and Δ*mamT* strains were cultivated for ~45 hours. Wild-type AMB-1 cultures were used as controls. The pH and optical density (OD) values were almost identical in all cultures of the three wild-type control, Δ*mamP* and Δ*mamT* AMB-1 strains (Table 3). Δ*mamP* cells showed limited iron incorporation normalized to the optical density, with a ~4-fold decrease compared to the wild-type (Table 3). Iron uptake by Δ*mamT* cells showed inconsistent values, with bulk iron concentration showing a slight increase during bacterial growth in two of the three replicates, and a decrease in the third replicate. We considered these data to be inconclusive. Finally, the Fe(II) / total Fe ratios were slightly lower in Δ*mamP* (0.11 ± 0.02) and Δ*mamT* (0.09 ± 0.02) compared to wild-type AMB-1 (0.16 ± 0.03).

Magnetic properties of AMB-1 cultures

After chemical analyses, bacteria were recovered and transferred into sample holders for magnetic analyses. Hysteresis loops were measured on whole bacterial populations (Fig. S1). Sample preparation was performed under anoxic conditions to prevent magnetite oxidation into maghemite [γ-Fe_2O_3]. Three magnetic parameters were extracted from hysteresis loops: the remanent magnetization (M_{rs}), the saturation magnetization (M_s) and the coercivity (H_c).

M_s depends only on the mass of magnetic material for a given phase, and is 92 emu per gram of magnetite (Zaitsev *et al*, 1999). Iron phases in MTB have been extensively described. In AMB-1 and MSR-1, as well as in the closely-related strain *Magnetospirillum magnetotacticum* MS-1, three iron species were evidenced both from bulk measurements and observations at the atomic scale: magnetite, ferrihydrite and Fe^{2+} (Frankel et al, 1983; Faivre et al, 2007; Baumgartner et al, 2013; Fdez-Gubieda et al, 2013; Uebe et al, 2019). Ferrihydrite and Fe^{2+} are paramagnetic at room-temperature, and do not to contribute to the M_s signal (Towe and Bardley, 1967; Aharoni, 2000; Wang et al, 2016). The M_s values thus provide accurate estimates of the mass of iron in magnetite, which is a ferrimagnetic material. M_{rs} corresponds to the remanent sample magnetization measured under an external magnetic field of zero, after exposing the sample to a saturating external field. M_{rs}/M_s ratio depends on particle size and organization, and is typically ranging between 0.43 and 0.50 in AMB-1 (Dunlop, 2002; Li *et al*, 2012). Finally, H_c is the magnetic field strength required to reduce the magnetization of the sample to zero after fully magnetizing it. Thus, H_c represents the capability of a magnetic material to resist demagnetization. It depends on the particle size, its shape, its magnetization, and its magnetocrystalline anisotropy.

Magnetic parameters calculated from hysteresis loops (Fig. S1) are given in Table 4 and Fig. 5. After 26 hours of growth, remanent (M_{rs}) and saturation (M_s) magnetizations were similar between the two experimental conditions (Figs. 5A and 5B). Similar to iron uptake patterns, most magnetite was precipitated between 26 and 46 hours of culturing in both conditions. No variation in M_{rs} and M_s was observed for longer time of culture. Final M_{rs} was $9.57 \pm 2.41 \times 10^{-4}$ emu and $2.09 \pm 0.57 \times 10^{-3}$ emu for AMB-1 cultivated with iron at 30 and 150 µM, respectively. Final M_s values were $2.06 \pm 0.44 \times 10^{-3}$ and $4.13 \pm 0.38 \times 10^{-3}$ emu for AMB-1 cultivated with iron at 30 and 150 µM, respectively. Knowing the magnetic moment of magnetite per unit of mass (92 emu/g), the M_s values were converted to a mass of iron

189 contained in magnetite. Results are given in Fig 3B. The maximum mass of iron in magnetite
190 measured was 0.082 ± 0.015 and 0.15 ± 0.015 mg per unit of optical density in AMB-1
191 cultivated with 30 and 150 μM of iron, respectively. From the remanent and saturation
192 magnetization values, we calculated the M_{rs} / M_s ratios. Almost identical values between the
193 two experimental conditions were observed: ~0.38, ~0.50 and ~0.50 after 26, 46 and 69 hours
194 of cultures, respectively (Fig. 5C). Coercivity showed a slightly different pattern, as it
195 progressively increased with time (Fig. 5D). After 26 hours of growth, the coercivity of
196 AMB-1 cultures was ~50 Oe for both initial iron concentrations. At longer growth times,
197 AMB-1 cultivated with 150 μM showed higher coercivities (180 ± 5 Oe and 224 ± 31 Oe for
198 46 and 69 hours of growth, respectively) than AMB-1 cultivated with 30 μM of iron (132 ± 8
199 Oe and 146 ± 26 Oe for 46 and 69 hours of growth, respectively).
200 We measured the mass of ferrimagnetic material in mutant AMB-1 strains following the same
201 approach. Jones and co-workers showed that nanoparticles produced in the Δ*mamP* and
202 Δ*mamT* cells also correspond to magnetite (Jones *et al*, 2015). Therefore, the same saturation
203 magnetization per unit of mass (92 emu/g) was used to calculate the mass of iron contained in
204 magnetite. Mutant AMB-1 strains showed altered magnetic properties (Table 5). The
205 remanent and saturation magnetizations in the Δ*mamP* strain were ~1 order of magnitude
206 lower than wild-type. Associated M_{rs} / M_s ratios showed lower values in Δ*mamP* AMB-1
207 (0.34 ± 0.09) compared to the wild-type control (0.46 ± 0.05). In Δ*mamT* AMB-1, the
208 saturation magnetization showed even lower values (~2 orders of magnitude lower than the
209 wild-type strain), while the remanent magnetization was ~0. Accordingly, M_{rs} / M_s ratios
210 corresponding to magnetite produced by Δ*mamT* cells were also ~0. Finally, coercivity
211 showed a ~3- to 4-fold decrease in the Δ*mamP* strain, and was close to zero in all Δ*mamT*
212 mutant samples.
213

Iron distribution in AMB-1 populations

Having determined the mass of iron in the different bacterial pools (*i.e.* magnetite and the rest of the cell), we finally wanted to quantify the iron distribution in AMB-1. The mass of iron in the lysate ($mass_{lysate}$, *i.e.* the fraction distinct from magnetite) was calculated from:

$$mass_{lysate} = mass_{cell} - mass_{magnetite} \quad \text{(Eq. 1)}$$

where $mass_{cell}$ and $mass_{magnetite}$ are the mass of iron contained in whole AMB-1 cells and in magnetite, respectively. $mass_{cell}$ was calculated from chemical assays, and $mass_{magnetite}$ was calculated from magnetic characterizations. The fraction of the total cellular iron contained in magnetite ($F_{magnetite}$, in %) was calculated from:

$$F_{magnetite} = \frac{mass_{cell} - mass_{lysate}}{mass_{cell}} \times 100 \quad \text{(Eq. 2)}$$

where $mass_{lysate}$ was calculated from Eq. 1.

Using results presented in Figs. 3A and 3B, we calculated the fraction of the total cellular iron contained in magnetite ($F_{magnetite}$ in Eq. 2) (Fig. 6). The mass of magnetite produced by wild-type AMB-1 cells cultivated at 30 and 150 µM was similar after 26 hours of growth, but iron uptake was 10 times higher under high-iron conditions. Therefore, magnetite corresponded to 11.2 ± 6% of the total cellular iron at this time point under low-iron conditions, but only 0.9 ± 0.3% of the cellular iron under high-iron conditions. In bacteria cultivated with 30 µM of iron, the fraction of cellular iron in magnetite increased to 21.9 ± 4 and 26 ± 3% after 46 and 69 hours of culture, respectively. In the 150 µM iron experimental conditions, it increased up to 14.5 ± 3 and 24.3 ± 5% after 46 and 69 hours of culture, respectively (Fig. 6). We note that all cells from every sample observed under the electron microscope contained magnetite crystals.

Therefore, our data cannot be explained by bacteria that accumulate iron without producing magnetite crystals. We manipulated and stored magnetite under anoxic conditions ($[O_2]$ < 1ppm) to prevent its oxidation into maghemite [γ-$Fe(III)_2O_3$] (Gallagher et al, 1968; Freer and O'Reilly, 1980; Rebodos and Vikesland, 2010). The saturation magnetization of maghemite is 60-80 emu per gram (Cornell and Schwertmann, 2004). Even if all magnetite became fully oxidized, the mass of iron precipitated as crystals in wild-type AMB-1 would be at most 40% higher as in Fig. 3B, and the mineral fraction of AMB-1 would represent no more than ~50-60% of the total cellular iron. In this case, our data would still support a significant pool of iron accumulating outside of magnetosome crystals. Finally, we ensured that all iron fractions in AMB-1 cultures were recovered (see materials and methods). Thus, a loss of iron during sample extraction and preparation cannot explain our results. Our data demonstrate that magnetite does not represent the major iron reservoir in AMB-1 under our experimental conditions.

To further demonstrate that iron accumulates outside of magnetite, we used additional wild-type AMB-1 cultures to assess the mean mass of magnetite per AMB-1 cell. Cell counting under a light microscope using a hemocytometer indicated an almost identical total number of cells for the two replicates: $8.48 \pm 2.21 \times 10^{10}$ and $8.39 \pm 2.26 \times 10^{10}$. The total mass of magnetite produced in these cultures and calculated from magnetic measurements was 0.025 and 0.024 mg. This yields a mean mass of iron contained in magnetite per cell of 2.11×10^{-7} and 2.10×10^{-7} ng for the two replicates, which corresponds to ~21 % of the bulk mass of iron measured in AMB-1 cells (Amor *et al*, 2019).

Additional wild-type cultures used as controls for experiments with the mutant strains showed similar results, with ~31 ± 8 % of the bulk cellular iron contained in magnetite. Magnetite in Δ*mamP* bacteria represented only 13 ± 12 % of the total cellular iron. All Δ*mamP* cells also produced magnetite under our experimental condition. Finally, the fraction of iron contained

in Δ*mamT* magnetite could not be determined because of inconclusive data on iron incorporation into these mutant bacteria (see above).

Subcellular localization and speciation of iron in AMB-1

Iron distribution assessments demonstrated that AMB-1 cells contain a large pool of iron, distinct from magnetite. However, they did not provide physical and chemical information about this additional pool. To determine the localization and speciation of iron in AMB-1, we used the fluorescence FRET Iron Probe 1 (FIP-1), an activity-based probe that allows the detection of labile Fe(II) (Aron et al, 2016). FIP-1 is made of a green (fluorescein) and a red (cyanine) fluorophores linked by an Fe(II)-cleavable endoperoxide. In the native FIP-1 state, the fluorescence energy of the excited fluorescein is transferred to the cyanine through a Fluorescence Resonance Energy Transfer (FRET) mechanism. In that case, only a red fluorescence signal can be observed. Upon reaction with labile Fe(II), the linker between the two fluorophores gets cleaved and a green fluorescence signal can be detected (Aron *et al*, 2016). To further constrain the speciation and subcellular localization of iron distinct from magnetite in AMB-1, wild-type, Δ*mamP* and Δ*mamT* cells were incubated with the FIP-1 probe and imaged via structured illumination microscopy. A mutant strain (ΔMAI) unable to form magnetosomes was used as a negative control (see supplementary materials).

A red fluorescence signal was observed in all samples, indicating the uptake of FIP-1 (Figs. 7, S4 and S5). A very weak green signal was observed in ΔMAI bacteria (Fig. S5), suggesting a lower labile iron concentration in these mutant cells. This observation is in good agreement with quantification of bulk iron in wild-type and ΔMAI bacteria (Amor *et al*, 2019). Both red and green fluorescence patterns showed intracellular heterogeneities, demonstrating that FIP-1 has been internalized into AMB-1. In wild-type bacteria, the green fluorescence signal was diffuse in the cytoplasm, although unstained spaces corresponding to PHB (Poly-β-

hydroxybutyrate, a carbon storage molecule) granules can be observed (Figs. 5 and S4). Green fluorescence signal also accumulated at the poles of the cell (Fig. S4). Such accumulation can be observed in dividing cells at the septum location (Fig. S6). Most of wild-type cells also showed a green fluorescence associated with the magnetosome chains (Fig. 7). AMB-1 produces fragmented chains of magnetite, with magnetosome vesicles spreading along the cell's long axis from pole to pole (Komeili *et al*, 2006; Arakaki *et al*, 2016). Unlike other *Magnetospirillum* strains such as MSR-1, apparent gaps between magnetite crystals can be observed from electron microscopy in AMB-1 (Fig. 1). These gaps correspond to empty magnetosome vesicles, containing no magnetite nanoparticles (Komeili *et al*, 2006; Arakaki *et al*, 2016). In our observations, the green fluorescence signals formed fragmented lines (*i.e.* similar to magnetite crystals) (Figs. 7 and S7). In some rare cases, the fluorescence lines extended almost from poles to poles (*i.e.* similar to magnetosome vesicles). As mentioned above, all bacteria observed with electron microscopy contained magnetite nanoparticles. Therefore, fluorescence patterns showing continuous lines cannot indicate empty vesicles in cells making no magnetite. Δ*mamP* showed all of the fluorescence features that have been observed in the wild-type strain (Figs. 7 and S8), whereas chains of magnetosomes could not be detected in Δ*mamT* AMB-1 using FIP-1 (Figs. 7 and S9).

Discussion

Mass balance experiments identified a large amount of iron distinct from magnetite in AMB-1, representing ~75 % of the bulk cellular iron in our experimental conditions. These results suggest a more complex picture for iron cycling and homeostasis in MTB than previously thought, as intracellular iron needs to be handled by the cell to prevent toxic effects.

Iron incorporation and distribution in AMB-1

Monitoring iron concentration and oxidation state in AMB-1 growth medium demonstrated that initial Fe(III) became progressively reduced into Fe(II) (Fig. 4). Accumulation of Fe(II) could result from active reduction by AMB-1, or illustrate respiration reactions depleting oxygen in AMB-1 medium. Our experimental setup cannot rule out one of the two possibilities, but we note that iron isotopes identified Fe(III) reduction within AMB-1 cells, and subsequent diffusion of intracellular Fe(II) to the growth medium (Amor *et al*, 2018).

Iron incorporation into wild-type AMB-1 was higher under high-iron conditions. When normalized to optical density, which is proportional to the concentration of cells in culture, iron uptake by AMB-1 after 26 h of culture was ~10-fold higher in the 150 μM experimental condition, compared to the 30 μM condition (Fig. 3). However, the mass of magnetite was similar in the two culture conditions (Fig. 3), indicating that the limiting step for biomineralization corresponds to magnetite precipitation and maturation, rather than iron uptake into the cell. Mass balance estimations were consistent in all wild-type cultures, and indicated that ~25 to ~30 % of the bulk cellular iron was contained in magnetite after 69h of growth. The mean mass of iron contained in magnetite per cell (~0.21 x 10^{-6} ng), estimated from cell counting and magnetic quantification using a VSM, corresponds to 21 % of the bulk iron content in AMB-1 determined by single-cell mass spectrometry analyses under the same experimental conditions (Amor *et al*, 2019). The results are almost identical to the mass balance estimations, and show that most of iron is contained in reservoir(s) distinct from magnetite. Moreover, the combination of electron microscopy and mass spectrometry measurements for quantification of iron content in AMB-1 evidenced a delay in magnetite formation as iron was incorporated into bacteria (Amor *et al*, 2019). This observation further supports accumulation of intracellular iron outside of magnetite.

The limited iron incorporation into Δ*mamP* AMB-1 suggests that magnetite biomineralization regulates iron assimilation. Whether this regulation corresponds to a direct or indirect mechanism remains unclear. A likely hypothesis could be that the iron accumulation capacity of the cell's fraction distinct from magnetite is limited. Once bacteria are fully loaded with iron, its sequestration into magnetite would be required for further assimilation. Such model would imply a two-step process for magnetite biomineralization, in which iron is first stored in the non-crystalline fraction of the cell, and then precipitated as magnetite. This is in good agreement with what has been proposed for iron cycling in AMB-1 and MSR-1 (Baumgartner *et al*, 2013; Fdez-Gubieda *et al*, 2013; Amor *et al*, 2018, 2019). The lack of MamP in the mutant strain could hamper iron precipitation in magnetosomes, and thus indirectly prevent further iron assimilation.

If 75 % of intracellular iron in AMB-1 is not stored in magnetite, the pool distinct from magnetite should represent ~0.75 x 10^{-6} ng of iron per cell (Amor *et al*, 2019). This mass is estimated to be 10 to 100-fold higher than the mass of iron in *Escherichia coli* cells (Andrews *et al*, 2003). The iron content in the ΔMAI AMB-1 strain, unable to form magnetosomes, was also estimated to be 5- to 10-fold higher than *E. coli* cells (Amor *et al*, 2019). Excess of free iron in the intracellular medium is toxic for cells (Andrews *et al*, 2003), which suggests efficient iron storage and detoxifying pathways in AMB-1. They could include ferritins, bacterioferritins and Dps proteins (Andrews *et al*, 2003; Uebe *et al*, 2010, 2019). Dps and bacterioferritins have recently been shown to protect MSR-1 from oxidative stress (Uebe *et al*, 2019), and phases corresponding to ferritin-like structures have been evidenced in AMB-1, MSR-1, and MS-1 strains using spectroscopic methodologies (Frankel et al, 1983; Faivre *et al*, 2007; Uebe *et al*, 2010; Baumgartner *et al*, 2013; Fdez-Gubieda *et al*, 2013; Uebe *et al*, 2019). Further iron toxicity assays in MTB and mutant strains lacking some of these iron-storing

proteins will help to better understand the capacity of MTB to tolerate such high intracellular iron concentrations.

Discrepancy with previous work

Our results clearly showed discrepancy with previous characterizations of iron species in the two magnetotactic strains AMB-1 and MSR-1 using X-ray absorption methodologies (Baumgartner *et al*, 2013; Fdez-Gubieda *et al*, 2013). In these two studies, time-course experiments were carried out in which AMB-1 or MSR-1 cells were cultivated without iron. When reaching saturation of cell density, iron was added to the growth medium to trigger magnetite biomineralization. Phases likely corresponding to ferrihydrite were first observed in both strains. When biomineralization was complete, magnetite was the sole iron carrier observed in bacteria. Since additional iron was detected by mass spectrometry and the protocol described in the present research, such discrepancy could suggest that X-ray absorption is not suitable for detection of iron that is not contained in magnetite or ferrihydrite. However, the important fraction of iron we identified in the iron pool distinct from magnetite rather suggests that the discrepancy arises from different experimental protocols. Moreover, recent work on MSR-1 also suggested that iron can be contained outside of magnetite in this strain (Berny *et al*, 2020). Iron-starving conditions can impact the iron cycling and homeostasis in MTB, as low-iron conditions have been shown to induce overexpression of iron acquisition systems in AMB-1 and MSR-1 (Suzuki *et al*, 2006; Wang *et al,* 2017). They might optimize the transfer of incorporated iron to magnetosomes for magnetite precipitation. Further X-ray absorption analyses with iron-starved bacteria and cells grown under standard conditions (*i.e.* as in the present work) will be needed to confirm this hypothesis.

The magnetic properties of AMB-1 cultures illustrate defects in magnetite biomineralization

In addition to the mass of magnetite produced in AMB-1 cultures, magnetic characterizations of bacterial samples provided important insights on the nanoparticle size and organization. AMB-1 produces stable single-domain magnetite nanoparticles (Li *et al*, 2012). The M_{rs} / M_s ratios corresponding to wild-type, mature AMB-1 magnetite typically range between 0.43 and 0.50 (Dunlop, 2020; Li *et al*, 2012). Smaller magnetite particles with crystal dimensions below 30 nm (for a width / length ratio of 0.2 or higher) are not magnetically stable at room-temperature, and fall within the superparamagnetic domain (Muxworthy and Williams, 2009). Their remanence magnetization is thus 0 at room-temperature, but their saturation magnetization remains unchanged for a given mass of magnetite. Very small superparamagnetic particles (<10 nm in length) would not reach complete saturation under the maximum external field we used (4 000 Oe) at room-temperature (Zuoquan et al, 2014). These particles represent less than 5% of the magnetite crystals observed under electron microscopy (Fig. S2). The underestimation of the saturation magnetization of these nanoparticles would be around 20 % (Zuoquan et al, 2014), meaning that the underestimation of the mass of magnetite would be below 1% and thus negligible. A mixing of stable single-domain and superparamagnetic particles would lead to lower M_{rs} / M_s ratios (Dunlop, 2002). M_{rs} / M_s ratios of ~0.38 observed after 26h of growth in wild-type cultures could thus reflect a mixing of mature and newly formed particles. Even though iron uptake was ~10-fold higher under high-iron conditions (Fig. 3), M_{rs} / M_s ratios in the two iron conditions were identical regardless of the initial iron concentration in the growth medium. As mentioned above, this suggests magnetite precipitation and growth as the limiting step for biomineralization in AMB-1. For longer culture times, M_{rs} / M_s ratios in wild-type AMB-1 were consistent with values ranging between 0.46 and 0.49 typical of AMB-1 magnetite (Li *et al*, 2012). Δ*mamP*

411 and Δ*mamT* AMB-1 also showed decreased M_{rs} / M_s ratios compared to the expected ~0.45
412 value. M_{rs} / M_s ratios in Δ*mamP* cultures of 0.34 are consistent with a mixing of stable single-
413 domain magnetite and smaller superparamagnetic particles as confirmed by electron
414 microscopy observations (Fig. 1). As mentioned above, very small superparamagnetic
415 particles would not reach saturation at room-temperature, leading to an underestimation of the
416 mass of magnetite of ~20%. In that case, our results would still support a large pool of iron
417 distinct from magnetite in the Δ*mamP* strain. Contrastingly, Δ*mamT* showed M_{rs} and M_{rs} / M_s
418 ratios of zero, which are both consistent with superparamagnetic particles produced in this
419 strain. Electron microscopy demonstrated that Δ*mamT* bacteria produced ~10 to 20-nm long
420 nanoparticles, in good agreement with the magnetic analyses (Muxworthy and Williams,
421 2009).
422 Finally, coercivity in wild-type cultures increased with time in both iron conditions.
423 Coercivity in stable single-domain particles such as those produced by MTB (Li et al, 2012)
424 depends on the particle size and shape, as well as the magnetocrystalline anisotropy which is
425 unlikely to change. Consistent H_c values between the two iron conditions after 26h of culture
426 suggest similar size and shape for magnetite crystals, in good agreement with iron uptake
427 patterns, remanent magnetization, and saturation magnetization (see above). For longer times
428 of culture, AMB-1 cultivated with iron at 150 μM showed higher coercivity. Since M_{rs} is
429 unchanged between these two cultures, this requires that the particles are larger or a different
430 shape under high-iron conditions. To test this hypothesis, we measured the magnetite length
431 and width distributions in both experimental conditions. Results are given in Figs. S2 and S3,
432 and show that the shape (length/width ratio) is almost identical in both experimental
433 conditions. However, bigger magnetite crystals were produced by AMB-1 cultivated with iron
434 at 150 μM (mean length of 38.46 nm) compared to the 30 μM condition (mean length of
435 32.03 nm), suggesting that increased coercivity results from bigger particles under high-iron

conditions. Lower coercivities in the mutant strains can also be explained by the presence of small superparamagnetic particles.

Localizing iron in AMB-1 cells

Two green fluorescence patterns were observed in AMB-1 cultures: a diffuse signal across the cell, and a signal that concentrated on the magnetosome chain. The SIM fluorescence microscope did not allow image acquisition of standard optical observation using white light, thus preventing estimation of the fraction of the total cells showing a fluorescence signal. Observation of magnetosome chains using FIP-1 shows that Fe(II) is addressed to magnetosomes during biomineralization. There is a possibility that FIP-1 indicates poorly crystalline Fe(II) at the magnetite surface, but our observations are best explained by Fe(II) being contained either in magnetite-containing or magnetite-free magnetosome vesicles (see below). It is unclear whether this Fe(II) would be contained inside magnetosomes, within the magnetosome membrane, or at the magnetosome surface. From high-resolution electron microscope analyses, Werckmann and collaborators proposed that iron could accumulate in the magnetosome membrane before its precipitation as magnetite (Werckmann *et al*, 2017). Our observations are in line with these results, and indicate that iron in the magnetosome membrane would at least be composed of Fe(II) species. Genes encoding for Fe(II) transporters have been found in the magnetosome gene island, and could transport Fe(II) across the magnetosome membrane for magnetite formation (Suzuki *et al*, 2006; Rong *et al*, 2008, 2012). Identical fluorescence patterns were observed in Δ*mamP* AMB-1, but not in the Δ*mamT* strain. The chain-like localization pattern in Δ*mamP* suggests that FIP-1 does not bind to magnetite, since this mutant strain produces only a few crystals per cell. It also indicates that Fe(II) is delivered to magnetosomes in the AMB-1 cells lacking MamP, and suggests that magnetite-free magnetosomes can be stained by FIP-1.

Another notable observation is an accumulation of fluorescence at the poles of AMB-1 cells showing a diffuse green signal. Whether such accumulation illustrates true biological mechanisms (flagellar apparatus, chemotaxis receptors, nitrate reductase complex, siderosomes, cell division) remains speculative, and additional work will be necessary to determine the significance of these observations (Müller et al, 2014; Popp *et al*, 2014; Alberge *et al*, 2015; Cunrath *et al*, 2015; Gasser *et al*, 2015).

Lastly, it is important to note that FIP-1 does not react with Fe(II) bound tightly to proteins as well as Fe(III) (Aron et al, 2016). It is likely that additional iron species distinct from magnetite are contained in AMB-1 cells, which include iron associated with heme domains (Siponen *et al*, 2013; Jones *et al*, 2015) or iron contained in storage proteins such as ferritins (Faivre et al, 2007; Uebe *et al*, 2019).

Implications for Earth sciences

It has been hypothesized that MTB deplete their environment in bioavailable iron by sequestering dissolved species into magnetite (Lin *et al*, 2014). Once the cell dies, MTB magnetite crystals can be trapped into sedimentary rocks, which effectively removes iron from the dissolved pool (Kopp and Kirschvink, 2008, Larrasoaña *et al*, 2014). MTB could thus prevent other living organisms from accessing an available source of iron. Some parameters are missing to accurately quantify the impact of MTB on the iron biogeochemical cycle. One of them is the speciation of iron in MTB, which controls its solubility. Our data demonstrated that most of iron in MTB exists as soluble species (*i.e.* Fe(II) and soluble Fe(III)-organic compounds), rather than magnetite. Iron sequestration in environmental MTB might thus be more limited than previously proposed (Amor *et al*, 2019). However, the discrepancy between the present work and the former X-ray absorption characterizations of iron in MTB (Baumgartner *et al*, 2013; Fdez-Gubieda *et al*, 2013) raises questions about the

environmental significance of our findings. Environmental MTB populations could experience varying iron conditions, and transition from iron-starving to iron-rich conditions similar to X-ray absorption experiments (Baumgartner *et al*, 2013; Fdez-Gubieda *et al*, 2013). In this case, most of intracellular iron could be contained in magnetite, with a limited soluble iron pool. Additional work constraining iron speciation in MTB that experience transitioning iron conditions, as well as in bacterial populations sampled from the environment, will be useful to further address the impact of MTB on the iron biogeochemical cycle.

Materials and Methods

Cultivation of wild-type and mutant AMB-1 strains

Magnetospirillum magneticum AMB-1 (ATCC 700264) was cultivated in 200 mL-bottles. The detailed composition of AMB-1 growth medium is given by Komeili and co-workers (Komeili *et al*, 2004). The sole iron source provided to AMB-1 cultures corresponded to Fe(III)-citrate, which was added to the growth media from an Fe(III)-citrate solution prepared by mixing Fe(III)Cl_3 (6 mM) and citric acid (12 mM) powders (Sigma-Aldrich) in Milli-Q water. The pH of the Fe(III)-citrate solution was set at 6.9 (*i.e.* same as AMB-1 growth medium) using NaOH. The initial Fe(III) concentration in AMB-1 growth medium was either 30 (*i.e.* standard concentration used in the ATCC medium) or 150 (*i.e.* the concentration used for isotope experiments) μM. The concentration of citrate and volume of cultures were kept constant in all experiments by adding an iron-free citrate solution (12 mM, pH 6.9) to AMB-1 cultures under low-iron conditions (30 μM). AMB-1 was cultivated in a glove box with controlled atmosphere (90% N_2, 10% O_2) at 30°C for three days. Each day, one bottle for each experimental condition was recovered for chemical and magnetic characterizations (see below). All measurements were carried out in triplicates (total of 18 bottles: two iron conditions, three time points, three replicates for each condition).

Two AMB-1 mutant strains were selected for additional experiments: the Δ*mamP* and Δ*mamT* strains lacking the genes encoding for the MamP and MamT proteins, respectively (Murat *et al*, 2010). MamP and MamT are magnetochrome proteins, a class of c-type cytochromes specific to MTB, which can bind iron via their heme domains (Siponen *et al*, 2013). Magnetochromes have been proposed to regulate the iron oxidation state in MTB (Siponen *et al*, 2013). The two mutant strains show biomineralization defects, which enable us to investigate the link between magnetite formation and iron uptake. The Δ*mamP* strain produces only a few crystals per cell resembling those produced by wild-type AMB-1, as well as a few additional small crystals (Fig. 1A-C). Δ*mamT* bacteria synthesize many small, elongated crystals (Fig.1D). The Δ*mamP* and Δ*mamT* strains have already been produced by our group (Murat *et al*, 2010). In AMB-1, *mamT* gene is located in the *mamAB* gene clusters of the MAI (termed R5 region in our previous work) downstream of three genes *mamQ*, *mamR* and *mamB* (Murat *et al*, 2010; Uebe and Schüler, 2016). These three genes are perfectly duplicated in the R9 region of the MAI, downstream of *mamT*. To avoid recombination between regions R5 and R9, the region R9 was deleted from Δ*mamT*. Therefore, bacteria used in this study correspond to the Δ*mamT*Δ*R9* strain, and are referred to as Δ*mamT*. We ensured that Δ*mamT* and Δ*mamT*Δ*R9* strains show similar biomineralization defects and both can be complimented with *mamT* expressed from a plasmid (Jones *et al*, 2015). Because the mutant strains produce less magnetite than wild-type AMB-1, as shown by the electron microscope observations (Fig. 1), we cultivated them with Fe(III)-citrate at 150 µM to measure iron uptake more accurately. The highest iron uptake by wild-type AMB-1 was observed at ~45 h of culture (see results). Accordingly, Δ*mamP* and Δ*mamT* strains were cultivated for ~45 hours in triplicates in 200-mL bottles (total of 9 bottles: 3 replicates for Δ*mamP* and Δ*mamT* and 3 replicates for wild-type bacteria used as a control).

536 **Transmission electron microscopy**

537 Bacteria were deposited on copper grids coated with a Formvar film, and observed with a
538 transmission electron microscope (FEI Tecnai 12) operating at 120 kV. From electron
539 microscopy observations, the length of magnetite nanoparticles produced by wild-type AMB-
540 1 cultivated for three days with Fe(III) at either 30 or 150 µM was measured using the ImageJ
541 software.

542

543 **Chemical measurements**

544 Bacterial iron uptake was quantified by measuring iron concentration in AMB-1 cultures at
545 initial (immediately after inoculation) and final (at the end of the bacterial culture) stages
546 using the ferrozine assay (Hunter *et al*, 2013). Ferrozine forms a purple-colored complex with
547 Fe(II), which can be determined spectrophotometrically. Total iron is then determined by total
548 reduction of iron in the sample with hydroxylamine hydrochloride and subsequent reaction
549 with ferrozine. Concentration of Fe(III) is calculated as the difference of total iron and Fe(II).
550 For each condition, pH and optical density at 400 nm (OD_{400nm}) were measured. Then, 1 mL
551 of culture was sampled and filtered (0.22-µm pore size; Acrodisc syringe filters,
552 polyethersulfone) at the initial and final stages. The Fe(II) and total iron concentrations were
553 measured using the ferrozine assay. The mass of iron taken up by AMB-1 was calculated
554 from iron depletion in each culture.
555 To demonstrate the reliability of the ferrozine assay for measuring iron depletion in AMB-1
556 cultures, we also prepared sterile growth media provided with Fe(III)-citrate at 30 or 150 µM
557 in 200-mL bottles. One mL of growth media was sampled and filtered (0.22-µm pore size;
558 Acrodisc syringe filters, polyethersulfone) after iron addition. Iron concentration and
559 speciation was measured with the ferrozine assay as described above. Sterile bottles were
560 incubated for 1, 2 or 3 days at 30°C in the glove box (90% N_2, 10% O_2). At the end of

561 experiment, 1 mL of growth media was recovered, filtered and the iron concentration and
562 speciation were measured using the ferrozine assay. Three replicates per condition were
563 prepared (18 samples total, as for wild-type bacterial cultures).
564
565 **Magnetic characterizations**
566 After chemical analyses, whole growth media were recovered and centrifuged (8,000 rpm, 10
567 min). Supernatants were discarded, and bacterial pellets corresponding to the entire bacterial
568 populations were dried in an anoxic chamber (98% N_2, 2% H_2, O_2 < 1 ppm) at room
569 temperature to prevent magnetite oxidation. We have already demonstrated that no significant
570 fraction of iron is adsorbed on AMB-1 cell surfaces (Amor *et al*, 2018). Virtually all iron
571 contained in bacterial pellets thus corresponds to intracellular iron. Once dried, whole
572 bacterial pellets were transferred into sample holders inside the anoxic chamber for
573 subsequent magnetic characterizations. Samples were kept in anoxic conditions until
574 magnetic analyses were performed. Hysteresis loops of magnetization versus applied
575 magnetic field were measured using a Vibrating-Sample Magnetometer (LakeShore VSM
576 7410) at room temperature. An integration time of 10 s per point was used.
577
578 **Iron mass balance**
579 To demonstrate the validity of our protocol and the accuracy of our measurements, we
580 ensured that all iron fractions were recovered and that no iron was lost during sample
581 extraction and preparation. Additional wild-type AMB-1 cultures were carried out in 200-mL
582 bottles for three days. One mL of growth medium was sampled and filtered before and after
583 cultures, and iron concentration was measured using the ferrozine assay as described above.
584 Cells were recovered by centrifugation (8,000 rpm, 10 min). The supernatant was discarded
585 and bacterial pellets were suspended in 100 µL of phosphate buffer (PBS). Cells were washed

three times in PBS and stored for subsequent measurements of total cellular iron mass (m_{cell}) using single-cell – inductively coupled plasma - mass spectrometry following a protocol previously published (Amor *et al*, 2019). Before mass-spectrometry measurements, PBS solution containing the bacteria was filtered to measure the potential mass of iron that leaked outside of the cells using high-resolution – inductively coupled plasma - mass spectrometry (m_{leaked}) (Amor *et al*, 2019). Iron recovery was assessed from the following mass balance equation:

$$m_{initial\ medium} = m_{residual\ medium} + m_{cell} + m_{leaked} \quad \text{(Eq. 3)}$$

where $m_{initial\ medium}$, and $m_{residual\ medium}$ are the mass of iron in the growth medium before and after AMB-1 cultures, respectively. m_{leaked} represented ~0.5 % of m_{cell} or less (Table 1). Mass balance estimations showed that iron recovery during sample preparation was ranging between 96 and 100% (Table S1), demonstrating the validity of our protocol. Therefore, a loss of iron pools such as magnetite could not explain our results.

Cell counting

To further demonstrate that wild-type AMB-1 incorporates more iron than needed to make its magnetite crystals, we chose an alternative approach to estimate the mean mass of magnetite per cell and to compare these results with available data on single-cell bulk iron content in AMB-1. Additional wild-type AMB-1 cultures (two replicates) were grown with Fe(III)-citrate at 150 μM. For each culture, the entire AMB-1 population was recovered with centrifugation, and the total mass of magnetite in a given population was determined from magnetic measurements as described above. The number of cells in the same populations was then calculated from direct cell counting using a hemocytometer under a light microscope.

Fifty counts were done for each AMB-1 culture. Finally, the mean mass of iron per cell was calculated from the total number of cells and the total mass of magnetite in each culture.

Detection and mapping of labile Fe(II) in AMB-1 using the FIP-1 fluorescent probe

The sensing mechanism for FIP-1 is inspired by antimalarial natural products and related therapeutics (Borstnik et al, 2002; Tang et al, 2005; Creek et al, 2007; Spangler et al, 2016). This reagent has been developed for use in mammalian cells and expanded in bioluminescent versions for mouse imaging (Aaron *et al*, 2017). We adapted the use of FIP-1 (Aron *et al*, 2016) for detection of Fe(II) in AMB-1. Wild-type and mutant AMB-1 strains were cultivated in 10 mL glass tubes until end of exponential phase / beginning of the stationary phase. Ten mL of growth medium were centrifuged, the supernatant was discarded, and cells were resuspended in 500 µL of PBS buffer. To ensure that all iron from the growth medium is removed, cells were centrifuged and washed in fresh PBS buffer three times. Finally, the three bacterial strains were mixed with a PBS solution containing EDTA (5mM, pH 6.9) for 10 min, centrifuged, and suspended in the FIP-1 solution (*i.e* FIP-1 at 1 mM in Hank's Balance Salt Solution) for 180 min at 30°C in the glove box (90% N_2, 10% O_2). All bacterial samples were observed by Structured Illumination Microscopy with a Carl Zeiss Elyra PS.1 Super Resolution fluorescence microscope, using red (excitation wavelength of 561 nm, emission wavelength of 570-620 nm) and green (excitation wavelength of 488 nm, emission wavelength of 495-550 nm) laser lines for the detection of the native and cleaved probe, respectively. Images were processed with the ImageJ software.

ACKNOWLEDGMENTS

AK and MA are supported by grants through the National Science Foundation (1504681) and National Institute of Health (R01GM084122 and R35GM127114). AC, CS and FH were

636 supported by the Director, office of Science, Office of Basic Energy Sciences, Materials
637 Sciences and Engineering Division, of the U.S. Department of Energy under Contract No.
638 DE-AC02-05-CH11231 within the Nonequilibrium Magnetic Materials Program (KC2204).
639 CJC and ATA were supported by a grant from the National Institute of Health
640 (R01GM079465). CJC is a CIFAR Senior Fellow. ATA thanks the NSF for a graduate
641 fellowship and was partially supported by an NIH Chemical Biology Interface Training Grant
642 (T32 GM066698). We thank Mickaël Tharaud for assistance with mass spectrometry analyses.
643 Part of this work was supported by IPGP multidisciplinary program PARI and by Region Ile-
644 de-France SESAME Grant no. 12015908.

References

Aharoni A. (2000) Introduction to the theory of ferromagnetism. Oxford University Press, Oxford.

Alberge F., Espinosa L., Seduk F., Sylvi L., Toci R., Walburger A., Magalon A. (2015) Dynamic subcellular localization of a respiratory complex controls bacterial respiration. *eLife* **4**, #e05357 doi: 10.7554/eLife.05357.

Amor M., Tharaud M., Gélabert A., Komeili A. (2019) Single-cell determination of iron content in magnetotactic bacteria: implications for the iron biogeochemical cycle. *Environ. Microbiol.* In press. https://doi.org/10. 1111/1462-2920.14708.

Amor M., Busigny V., Louvat P., Tharaud M., Gélabert A., Cartigny P., Carlut J., Isambert A., Durand-Dubief M., Ona-Nguema G., Alphandéry E., Chebbi I., Guyot F. (2018) Iron uptake and magnetite biomineralization in the magnetotactic bacterium *Magnetospirillum magneticum* strain AMB-1: an iron isotope study. *Geochim. Cosmochim. Acta* **232**, 225-243.

Amor M., Busigny V., Louvat P., Gélabert A., Cartigny P., Durand-Dubief M., Ona-Nguema G., Alphandéry E., Chebbi I., Guyot F. (2016) Mass-dependent and -independent signature of Fe isotopes in magnetotactic bacteria. *Science* **352**, 705-708.

Andrews S. C., Robinson A. K., Rodríguez-Quiñones F. (2003) Bacterial iron homeostasis. *FEMS Microbiol. Rev.* **27**, 215-237.

Arakaki A., Kikuchi D., Tanaka M., Yamagishi A., Yoda T., Matsunaga T. (2016) Comparative subcellular localization analysis of magnetosome proteins reveals a unique localization behavior of Mms6 protein onto magnetite crystals. *J. Bacteriol.* **198**, 2794-2802.

668 Aron A. T., Loeehr M. O., Bogena J., Chang C. J. (2016) An endoperoxide reactivity-based
669 FRET Probe for ratiometric fluorescence imaging of labile iron pools in living cells. *J. Am.*
670 *Chem. Soc.* **138**, 14338-14346.
671 Aron A. T., Heffern M. C., Lonergan Z. R., Vander Wal M. N., Blank B. R., Spangler B.,
672 Zhang Y., Park H. M., Stahl A., Renslo A. R., Skaar E. P., Chang C. J. (2017) *In vivo*
673 bioluminescence imaging of labile iron accumulation in a murine model of *Acinobacter*
674 *baumannii* infection. *Proc. Natl. Acad. Sci. U. S. A.* **114**, 12669-12674.
675 Baumgartner J., Morin G., Menguy N., Perez Gonzalez T., Widdrat M., Cosmidis J., Faivre D.
676 (2013) Magnetotactic bacteria form magnetite from a phosphate-rich ferric hydroxide via
677 nanometric ferric (oxyhydr)oxide intermediates. *Proc. Natl. Acad. Sci. U. S. A.* **110**,
678 14883-14888.
679 Berny C., Le Fèvre R., Guyot F., Blondeau K., Guizonne C., Rousseau E., Bayan N.,
680 Alphandéry E. (2020) A method for producing highly pure magnetosomes in large quantity
681 for medical applications using *Magnetospirillum gryphiswaldense* MSR-1 magnetotactic
682 bacteria amplified in minimal growth media. *Front. Bioeng. Biotechnol.* **8**, 16. Doi:
683 10;3389/fbioe.2020.00016.
684 Borstnik K., Paik I. H., Shapiro T. A., Posner G. H. (2002) Antimalarial chemotherapeutic
685 peroxides: artemisinin, yingzhaosu A and related compounds. *Int. J. Parasitol.* **32**, 1661-
686 1667.
687 Cornell R. M., Schwertmann U. (2013) The iron oxides: structure, properties, reactions,
688 occurrences and uses, second edition. Wiley-VCH Verlag GmbH & Co. KGaA.
689 Creek D. J., Charman W. N., Chiu F. C., Prankerd R. J., McCullough K. J., Dong Y.,
690 Vennerstrom J. L., Charman S. A. (2007) Iron-mediated degradation kinetics of substituted
691 dispiro-1,2,4-trioxolane antimalarials. *J. Pharm. Sci.* **96**, 2945-2956.

692 Cunrath O., Gasser V., Hoegy F., Reimmann C., Guillon L., Schalk I. J. (2015) A cell
693 biological view of the siderophore pyochelin iron uptake pathway in *Pseudomonas*
694 *aeruginosa*. *Environ. Microbiol.* **17**, 171-185.
695 Dunlop D. J. (2002) Theory and application of the Day plot (M_{rs}/M_s versus H_{cr}/H_c): 1/
696 Theoretical curves and tests using titanomagnetite data. *J. Geophys. Res.* **107**, doi:
697 10.1029/2001JB000486.
698 Faivre D., Böttger L. H., Matzanke B. F., Schüler D. (2007) Intracellular magnetite
699 biomineralization in bacteria proceeds by a distinct pathway involving membrane-bound
700 ferritin and an iron(II) species. *Ang. Chem. Int. Ed.* **46**, 8495-8499.
701 Fdez-Gubieda M. L., Muela A., Alonso J., García-Prieto A., Olivi L., Fernández-Pacheco R.,
702 Barandiarán J. M. (2013) Magnetite biomineralization in *Magnetospirillum*
703 *gryphiswaldense*: time-resolved magnetic and structural studies. *ACS Nano* **7**, 3297-3305.
704 Frankel R. B., Papaefthymiou G. C., Blakemore R. P., O'Brien W. (1983) Fe_3O_4 precipitation
705 in magnetotactic bacteria. *Biochim. Biophys. Acta.* **763**, 147-159.
706 Freer W., O'Reilly R. (1980) The diffusion of Fe^{2+} ions in spinels with relevance to the
707 process of maghemitization. *Mineral. Mag.* **43**, 889-899.
708 Gallagher K. J., Feitknecht W., Mannweiler U. (1968) Mechanism of oxidation of magnetite
709 to γ-Fe_2O_3. *Nature* **217**, 1118-1121.
710 Gasser V., Guillon L., Cunrath O., Schalk I. J. (2015) Cellular organization of siderophore
711 biosynthesis in *Pseudomonas aeruginosa*: evidence for siderosomes. *J. Inorg. Biochem.*
712 **148**, 27-34.
713 Hunter R. C., Asfour F., Dingemans J., Osuna B. L., Samad T., Malfroot A., Cornelis P.,
714 Newman D. K. (2013) Ferrous iron is a significant component of bioavailable iron in
715 cystic fibrosis airways. *mBio* **4**, e00557-13.

716 Jones S. R., Wilson T. D., Brown M. E., Rahn-Lee L., Yu Y., Fredriksen L. L., Ozyamak E.,
717 Komeili A., Chang M. C. Y. (2015) Genetic and biochemical investigations of the role of
718 MamP in redox control of iron biomineralization in *Magnetospirillum magneticum*. *Proc.*
719 *Natl. Acad. Sci. U. S. A.* **112**, 3904-3909.
720 Komeili A., Li Z., Newman D. K., Jensen G. J. (2006) Magnetosomes are cell membrane
721 invaginations organized by the actin-like protein MamK. *Science* **31**, 242-245.
722 Komeili A., Vali H., Beveridge T. J., Newmann D. K. (2004) Magnetosome formation are
723 present before magnetite formation, and MamA is required for their activation. *Proc. Natl.*
724 *Acad. Sci. U. S. A.* **101**, 3839-3844.
725 Kopp R. E., Kirschvink J. L. (2008) The identification and biogeochemical interpretation of
726 fossil magnetotactic bacteria. *Earth-Sci. Rev.* **86**, 42-61.
727 Larrasoaña J. C., Liu Q., Hu P., Roberts A. P., Mata P., Civis J., Sierro F. J., Pérez-Asensio J.
728 N. (2014) Paleomagnetic and paleoenvironmental implications of magnetofossil
729 occurences in late Miocene marine sediments from the Guadalquivir basin, SW Spain.
730 *Front. Microbiol.* **5**, #71 doi: 10.3389/fmicb.2014.00071.
731 Li J., Pan Y., Chen G., Liu Q., Tian L., Lin W. (2009) Magnetite magnetosome and
732 fragmental chain formation of *Magnetospirillum magneticum* AMB-1: transmission
733 electron microscopy and magnetic observations. *Geophys. J. Int.* **177**, 33-42.
734 Li J., Wu W., Liu Q., Pan Y. (2012) Magnetic anisotropy, magnetostatic interactions and
735 identification of magnetofossils. *Geochem. Geophys. Geosyst.* **13**, #Q10Z51. doi:
736 10.1029/2012GC004384.
737 Lin W., Bazylinski D. A., Xiao T., Wu L.-F., Pan Y. (2014) Life with compass: diversity and
738 biogeography of magnetotactic bacteria. *Environ. Microbiol.* **16**, 2646-2658.

739 McCausland H. C., Komeili A. (2020) Magnetic genes: studying the genetics of
740 biomineralization in magnetotactic bacteria. *PLoS Genet.* **16**, e1008499. Doi:
741 10.1371/journal.pgen.1008499.
742 Meister M. (2016) Physical limits to magnetogenetics. *eLife* **5**, e17210. doi:
743 10.7554/eLife.17210.
744 Müller F., Raschdorf O., Nudelman H., Messerer M., Katzmann E., Plitzko J. M., Zarivach R.,
745 Schüler D. (2013) The FtsZ-like protein FtsZm of *Magnetospirillum gryphiswaldense*
746 likely interacts with its generic homolog and is required for biomineralization under nitrate
747 deprivation. *J. Bacteriol.* **196**, 650-659.
748 Murat D., Quinlan A., Vali H., Komeili A. (2010) Comprehensive genetic dissection of the
749 magnetosome gene island reveals the step-wise assembly of a prokaryotic organelle. *Proc.*
750 *Natl. Acad. Sci. U. S. A.* **107**, 5593-5598.
751 Muxworthy A. R., Williams W. (2009) Critical superparamagnetic/single-domain grain sizes
752 in interacting magnetite particles: implications for magnetosome crystals. *J. R. Soc.*
753 *Interface* **6**, 1207-1212.
754 Popp F., Armitage J. P., Schüler D. (2014) Polarity of bacterial magnetotaxis is controlled by
755 aerotaxis through a common sensory pathway. *Nat. Commun.* **5**, #5398 doi:
756 10.1038/ncomms6398.
757 Rebodos R. L., Vikesland P. J. (2010) Effects of oxidation on the magnetization of
758 nanoparticulate magnetite. *Langmuir* **26**, 16745-16753.
759 Rong C., Zhang C., Zhang Y., Qi L., Yang J., Guan G., Li Y., Li J. (2012) FeoB2 functions in
760 magnetosome formation and oxidative stress protection in *Magnetospirillum*
761 *gryphiswaldense* strain MSR-1. *J. Bacteriol.* **194**, 3972-3976.

762 Rong C., Huang Y., Zhang W., Jiang W., Li Y., Li J. (2008) Ferrous iron transport protein B
763 gene (*feoB1*) plays an accessory role in magnetosome formation in *Magnetospirillum*
764 *gryphiswaldense* strain MSR-1. *Res. Microbiol.* **159**, 530-536.
765 Siponen M. I., Legrand P., Widdrat M., Jones S. R., Zhang W.-J., Chang M. C. Y., Faivre D.,
766 Arnoux P., Pignol D. (2013) Structural insight into magnetochrome-mediated magnetite
767 biomineralization. *Nature* **502**, 681-684.
768 Spangler B., Morgan C. W., Fontaine S. D., Vander Wal M. N., Chang C. J., Wells J. A.,
769 Rensio A. R. (2016) A reactivity-based probe of the intracellular labile ferrous iron pool.
770 *Nat. Chem. Biol.* **12**, 680-685.
771 Suzuki T., Okamura Y., Calugay R. J., Takeyama H., Matsunaga T. (2006) Global gene
772 expression analysis of iron-inducible genes in *Magnetospirillum magneticum* AMB-1. *J.*
773 *Bacteriol.* **188**, 2275-2279.
774 Tang Y. Q., Dong Y. X., Wang X. F., Sriraghavan K., Wood J. K., Vennerstrom J. L. (2005)
775 Dispiro-1,2,4-trioxane analogues of a prototype dispiro-1,2,4-trioxolane: mechanistic
776 comparators for artemisinin in the context of reaction pathways with iron(II). *J. Org. Chem.*
777 **70**, 5103-5110.
778 Towe K. M., Bradley W. F. (1967) Mineralogical constitution of colloidal 'hydrous ferric
779 oxides". *J. Colloid. Interf. Sci*. **24**, 384-392.
780 Uebe R., Ahrens F., Stang J., Jäger K., Böttger L. H., Schmidt C., Matzanke B. F., Schüler D.
781 (2019) Bacterioferritin of *Magnetospirillum gryphiswaldense* is a heterotetraeicosameric
782 complex composed of functionally distinct subunits but is not involved in magnetite
783 biomineralization. *mBio* **10**, #e02795-18 doi: 10.1128/mBio.02795-18.
784 Uebe R., Schüler D. (2016) Magnetosome biogenesis in magnetotactic bacteria. *Nature Rev.*
785 *Microbiol.* **14**, 621-637.

786 Uebe R., Voigt B., Schweder T., Albrecht D., Katzmann E., Lang C., Böttger L., Matzanke B.,
787 Schüler D. Deletion of a *fur*-like gene affects iron homeostasis and magnetosome
788 formation in *Magnetospirillum gryphiswaldense. J. Bacteriol.* **192**, 4192-4204.
789 Wang Q., Wang X., Zhang W., Li X., Zhou Y., Li D., Wang Y., Tian J., Jiang W., Zhang Z.,
790 Peng Y., Wang L., Li Y., Li J. (2017) Physiological characteristics of *Magnetospirillum*
791 *gryphiswaldense* MSR-1 that control cell growth under high-iron and low-oxygen
792 conditions. *Sci. Rep.* **7**: 2800. Doi: 10.1038/s41598-017-03012-4.
793 Wang X., Zhu M., Koopal L. K., Li W., Xu W., Liu F., Zhang J., Liu Q., Feng X., Sparks D.
794 L. (2016) Effects of crystallite size on the structure and magnetism of ferrihydrite. *Environ.*
795 *Sci.: Nano.* **3**, 190-202.
796 Werckmann J., Cypriano J., Lefèvre C. T., Dembelé K., Ersen O., Bazylinski D. A., Lins U.,
797 Farina M. (2017) Localized iron accumulation precedes nucleation and growth of
798 magnetite crystals in magnetotactic bacteria. *Sci. Rep.* **7**, #8290 doi:10.1038/s41598-017-
799 08994-9.
800 Zaitsev V. S., Filimonov D. S., Presnyakov I. A., Gambino R. J., Chu B. (1999) Physical and
801 chemical properties of magnetite and magnetite-polymer nanoparticles and their colloidal
802 dispersions. *J. Colloid Interface Sci.* **212**, 49-57.
803 Zuoquan Z., Sun Q., Zhong J., Qihua Y., Li H., Cheng D., Liang B., Shuai X. (2014)
804 Magnetic resonance imaging-visible and pH-sensitive polymeric micelles for tumor
805 targeted drug delivery. *J. Biomed. Nanotechnol.* **10**, 216-226.

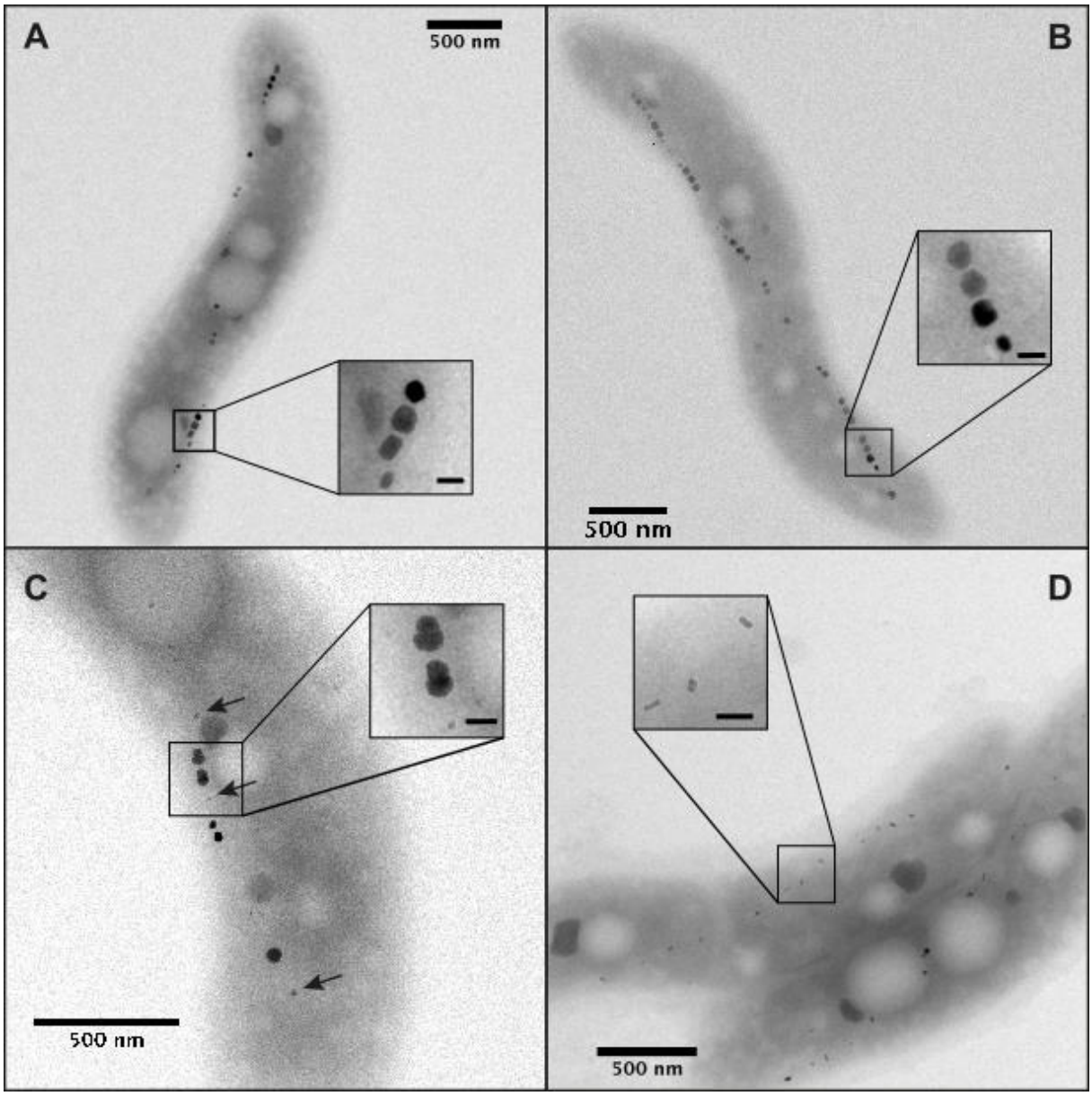

FIG 1 Transmission electron observations of wild-type AMB-1 cells cultivated for three days with initial iron concentrations in the growth medium of (A) 30 or (B) 150 μM, and (C) Δ*mamP* and (D) Δ*mamT*Δ*R9* (referred to as Δ*mamT*) AMB-1 strains cultivated with Fe(III)-citrate at 150 μM. Arrows in (C) indicate small nanoparticles produced by the Δ*mamP* bacteria. Scale bars (insets) = 50 nm.

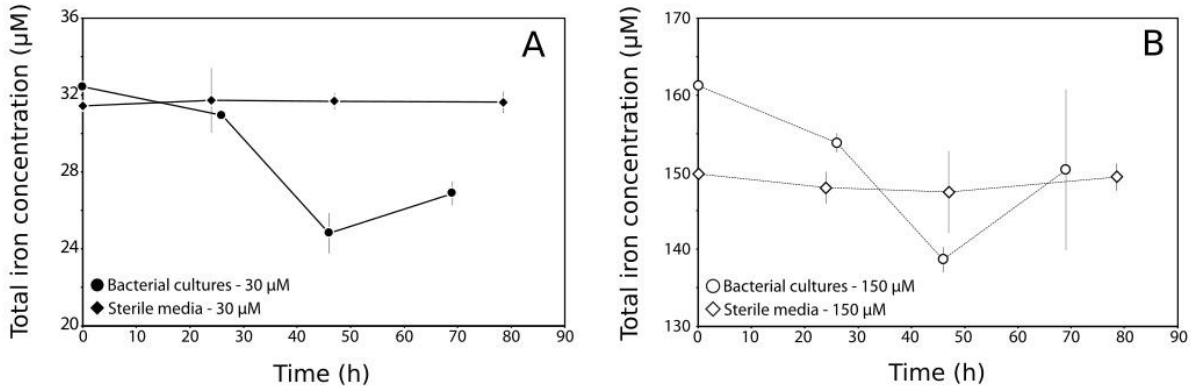

812

813 **FIG 2** Total iron concentration in (circles) AMB-1 and (diamonds) sterile media provided

814 with iron at (A) 30 or (B) 150 µM. Each point corresponds to the mean value of 3 replicates ±

815 1SD. Note the different y-axes.

816

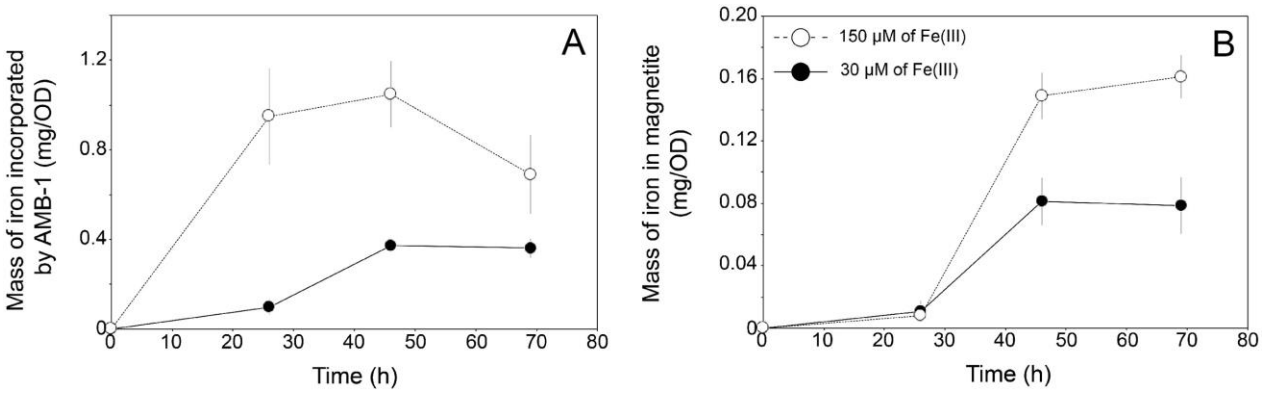

FIG 3 Mass of iron (A) taken up by AMB-1 and (B) contained in magnetite during bacterial growth. All values are normalized to optical densities (OD), which is proportional to the cell biomass. Thus, different cell densities cannot explain discrepancies in iron uptake. Each point corresponds to the mean value of three replicates ± 1SD. Note the different y-axes. Black circles and open symbols refer to cultures with an initial iron concentration of 30 and 150 µM, respectively.

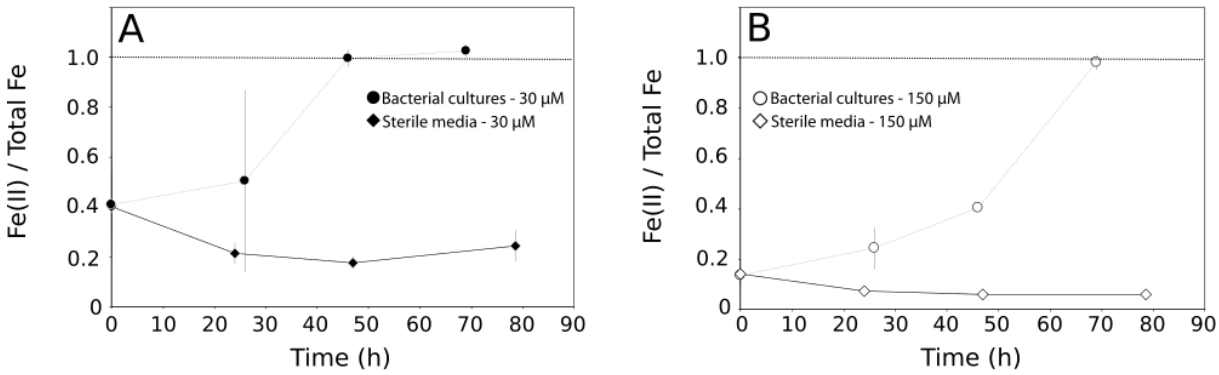

825

826 **FIG 4** Iron speciation in (circles) AMB-1 and (diamonds) sterile media provided with iron at

827 (A) 30 or (B) 150 µM. Each point corresponds to the mean value of 3 replicates ± 1SD.

828

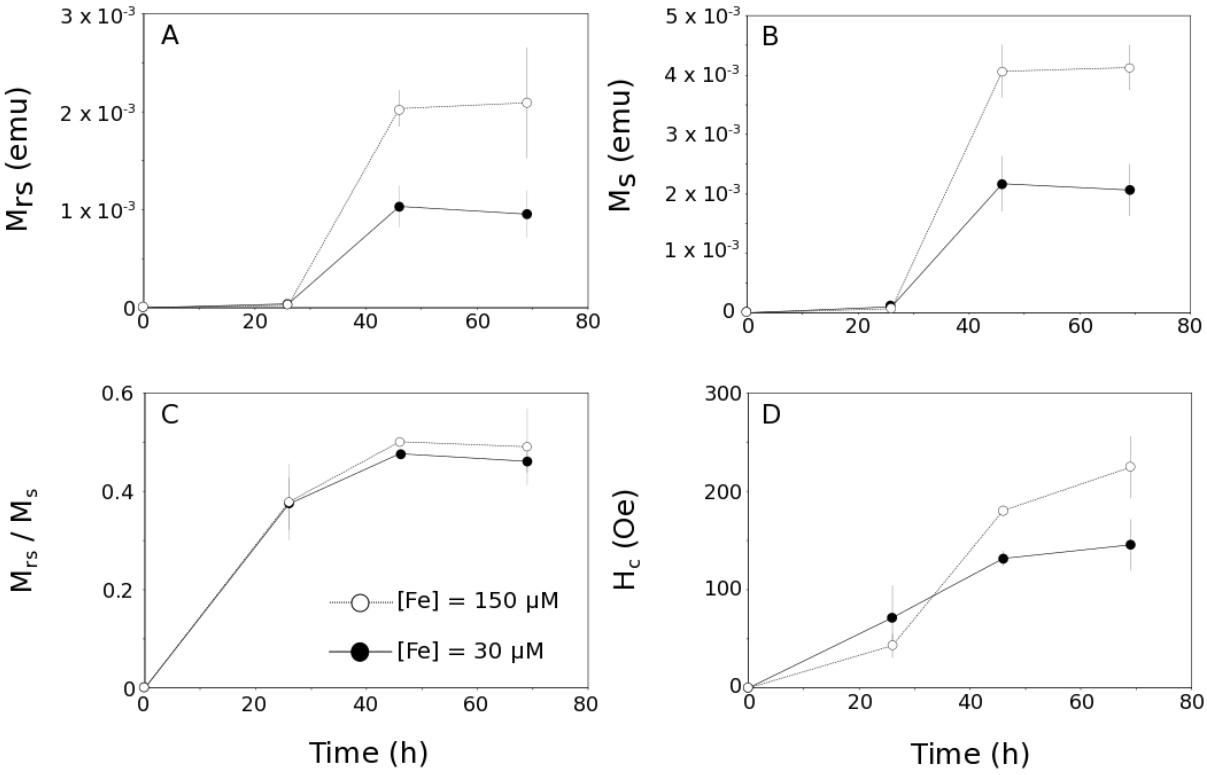

829

830 **FIG 5** (A) Remanent magnetization (M_{rs}), (B) saturation magnetization (M_s), (C) coercivity
831 (H_c) and (D) M_{rs} / M_s ratios for the studied AMB-1 cultures. Each point corresponds to the
832 mean value of three replicates ± 1SD. Black circles and open symbols refer to cultures with
833 an initial iron concentration of 30 and 150 µM, respectively.

834

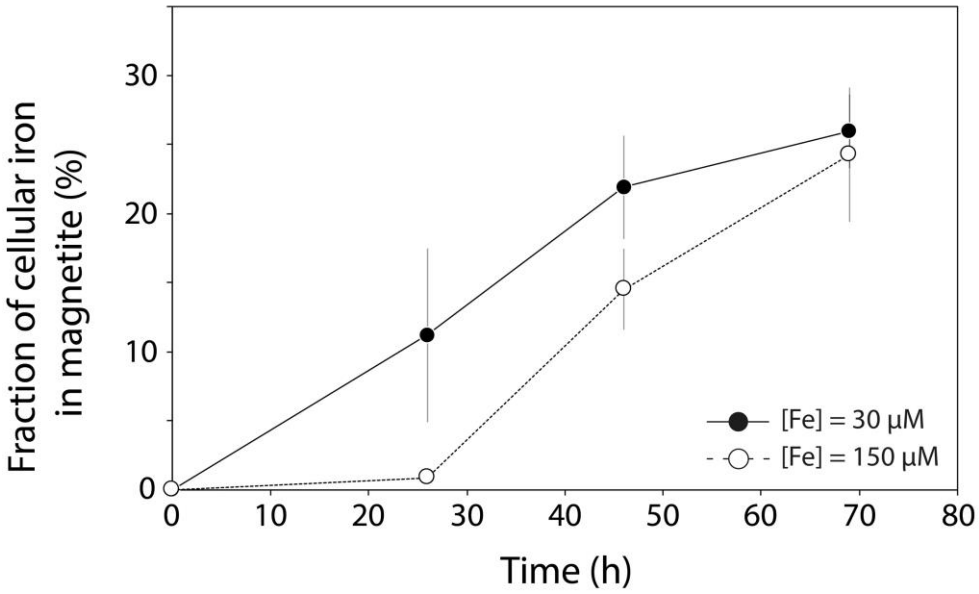

835

836 **FIG 6** Relative fraction of the total cellular iron contained in magnetite. Each point
837 corresponds to the mean value of three replicates ± 1SD. Black circles and open symbols refer
838 to cultures with an initial iron concentration of 30 and 150 µM, respectively.

839

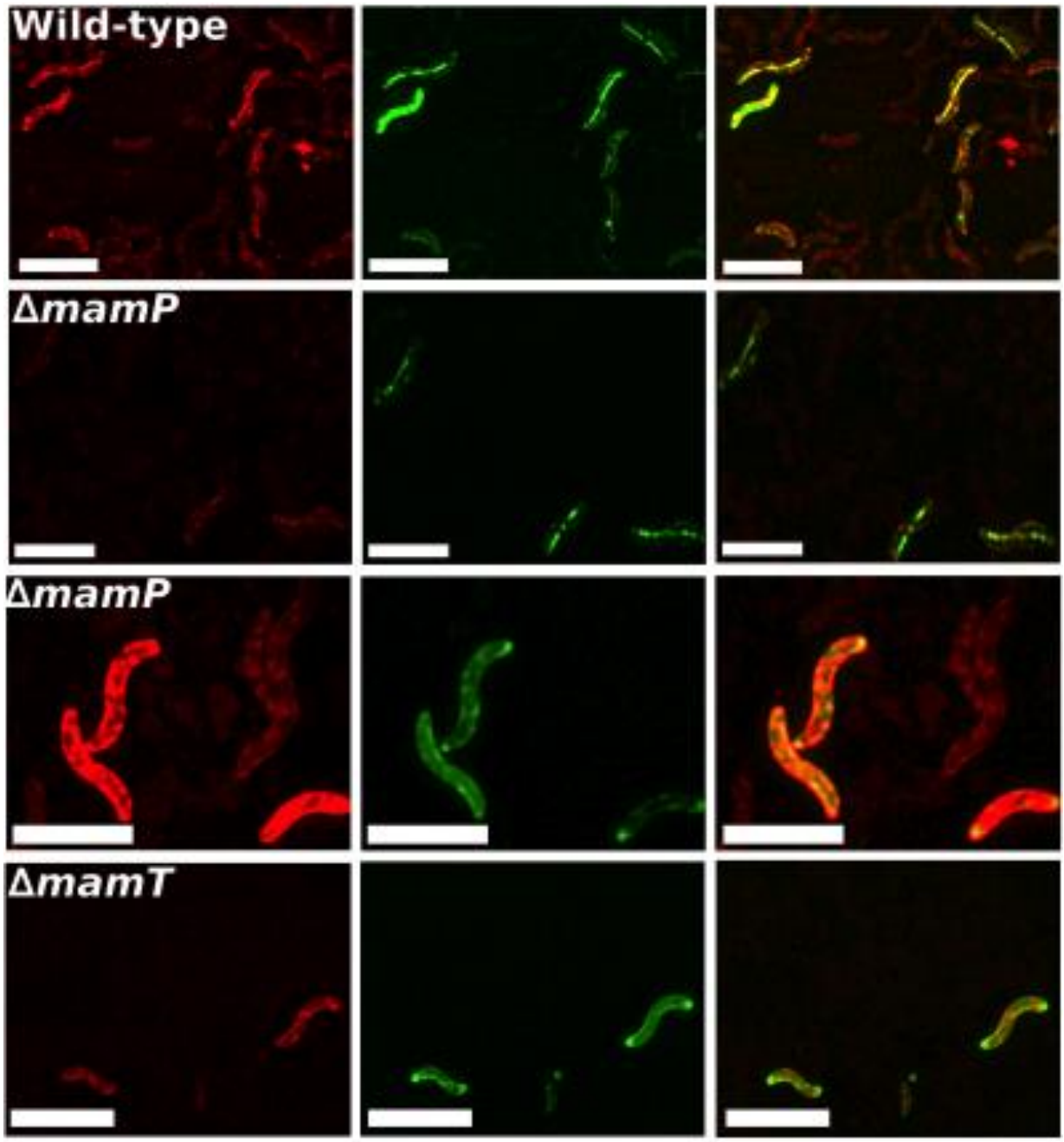

FIG 7 Red (left panels), green (center panels) and merged (right panels) fluorescence images of wild-type, Δ*mamP* and Δ*mamT* AMB-1 incubated with FIP-1 for 180 min. The two Δ*mamP* panels show the two fluorescence patterns (diffuse and located to the magnetosome chains, as in wild-type) observed in the populations. Scale bars = 4 microns. Additional pictures are available in the supplementary materials.

846 **Table 1** Fe(II) and total iron concentration in initial and final sterile growth media.
847

Time of culture (h)	Volume of culture (mL)	Initial [Fe(II)] (μM)	Initial [Fe] (μM)	Final [Fe(II)] (μM)	Final [Fe] (μM)
[Fe] = 30 μM					
24 #1	190	21.41	33.07	8.53	33.59
24 #2	190	18.97	31.50	6.61	30.28
24 #3	190	18.27	32.02	5.39	31.33
47 #1	190	14.44	30.46	6.70	32.10
47 #2	190	12.18	32.20	5.29	31.22
47 #3	190	11.14	30.46	4.94	31.75
78.5 #1	190	8.70	31.15	9.88	31.22
78.5 #2	190	5.22	30.98	6.88	32.28
78.5 #3	190	4.35	31.15	6.53	31.39
[Fe] = 150 μM					
24 #1	190	33.07	151.58	11.83	146.53
24 #2	190	29.59	151.06	10.44	149.49
24 #3	190	30.63	150.71	-	-
47 #1	190	24.02	152.45	10.93	153.27
47 #2	190	22.28	139.57	8.64	146.39
47 #3	190	19.14	151.41	7.05	142.68
78.5 #1	190	12.53	153.49	10.41	147.80
78.5 #2	190	11.66	149.49	9.70	149.03
78.5 #3	190	8.70	148.45	7.58	151.33

848

Table 2 Fe(II) and total iron concentration in the growth medium before and after AMB-1 cultures, and final optical density at 400 nm (OD_{400nm}) and pH values of bacterial cultures (starting pH = 6.9).

Time of culture (h)	Volume of culture (mL)	Initial [Fe(II)] (μM)	Initial [Fe] (μM)	Final OD_{400nm} (AU)	Final pH	Final [Fe(II)] (μM)	Final [Fe] (μM)
[Fe] = 30 μM							
26 #1	185	16.87	31.36	0.067	6.95	7.29	30.94
26 #2	185	17.24	31.72	0.060	6.91	11.03	30.94
26 #3	185	17.05	31.72	0.083	7.01	28.45	30.94
46 #1	185	14.12	32.46	0.209	7.26	24.99	24.30
46 #2	185	13.94	32.82	0.202	7.34	24.99	26.03
46 #3	185	14.85	31.72	0.214	7.26	24.12	24.12
69 #1	185	8.80	33.19	0.212	7.42	28.12	27.42
69 #2	185	8.44	33.19	0.203	7.44	28.47	27.07
69 #3	185	7.52	33.74	0.204	7.42	26.20	26.20
[Fe] = 150 μM							
26 #1	185	29.16	162.65	0.069	7.03	51.57	154.89
26 #2	185	26.96	157.15	0.067	6.94	35.21	152.40
26 #3	185	26.41	159.35	0.056	6.94	25.96	154.18
46 #1	185	26.77	161.00	0.215	7.18	57.80	140.24
46 #2	185	23.29	158.25	0.215	7.28	54.15	138.85
46 #3	185	20.90	161.73	0.211	7.30	56.58	136.94
69 #1	185	15.95	160.27	0.197	7.48	143.39	146.88
69 #2	175	15.95	172.00	0.202	7.50	154.57	162.08
69 #3	185	14.12	158.80	0.202	7.50	143.74	141.99

Table 3 Fe(II) and total iron concentration in the growth medium before and after mutant AMB-1 cultures, and final optical density at 400 nm (OD_{400nm}) and pH values of bacterial cultures (starting pH = 6.9). Additional wild-type cultures were used as a control condition.

Time of culture (h)	Volume of culture (mL)	Initial [Fe(II)] (μM)	Initial [Fe] (μM)	Final OD_{400nm} (AU)	Final pH	Final [Fe(II)] (μM)	Final [Fe] (μM)
Wild-type							
43 #1	178	25.08	150.30	0.250	7.30	26.23	145.78
43 #2	173	22.85	155.69	0.252	7.24	25.23	150.59
43 #3	167	23.22	164.05	0.255	7.40	19.42	151.99
Δ*mamP*							
43 #1	171	21.55	159.59	0.261	7.32	21.43	158.20
43 #2	174	19.32	161.27	0.252	7.35	18.23	161.00
43 #3	170	18.21	162.75	0.261	7.33	14.42	159.20
Δ*mamT*							
43 #1	175	16.72	157.92	0.248	7.34	15.02	158.20
43 #2	177	15.42	153.23	0.280	7.35	15.62	148.29
43 #3	164	14.31	169.44	0.252	7.39	10.21	172.22

859 **Table 4** Remanent magnetization (M_{rs}), saturation magnetization (M_s), coercivity (H_c) and
860 M_{rs}/M_s ratios of wild-type AMB-1.
861

Time of culture (h)	M_{rs} (emu)	M_s (emu)	H_c (Oe)	M_{rs}/M_s
[Fe] = 30 μM				
26 #1	1.74×10^{-5}	4.06×10^{-5}	75.50	0.43
26 #2	2.55×10^{-5}	7.88×10^{-5}	37.02	0.32
26 #3	7.03×10^{-5}	1.89×10^{-4}	102.17	0.37
46 #1	1.08×10^{-3}	2.23×10^{-3}	138.02	0.48
46 #2	8.00×10^{-4}	1.68×10^{-3}	123.28	0.48
46 #3	1.22×10^{-3}	2.60×10^{-3}	134.23	0.47
69 #1	6.80×10^{-4}	1.57×10^{-3}	115.97	0.43
69 #2	1.07×10^{-3}	2.24×10^{-3}	156.12	0.48
69 #3	1.12×10^{-3}	2.39×10^{-3}	164.70	0.47
[Fe] = 150 μM				
26 #1	5.19×10^{-5}	1.12×10^{-4}	56.81	0.46
26 #2	1.99×10^{-5}	6.42×10^{-5}	34.87	0.31
26 #3	1.15×10^{-5}	3.18×10^{-5}	37.50	0.36
46 #1	2.23×10^{-3}	4.52×10^{-3}	186.19	0.49
46 #2	2.01×10^{-3}	4.03×10^{-3}	175.58	0.50
46 #3	1.86×10^{-3}	3.64×10^{-3}	179.27	0.51
69 #1	-	-	-	-
69 #2	1.69×10^{-3}	3.89×10^{-3}	202.27	0.43
69 #3	2.49×10^{-3}	4.57×10^{-3}	246.70	0.55

862

Table 5 Remanent magnetization (M_{rs}), saturation magnetization (M_s), coercivity (H_c) and M_{rs}/M_s ratios of whole mutant cells recovered after cultures. Additional wild-type cultures were used as a control condition.

Time of culture (h)	M_{rs} (emu)	M_s (emu)	H_c (Oe)	M_{rs}/M_s
Wild-type				
43 #1	9.07×10^{-4}	2.29×10^{-3}	128.62	0.40
43 #2	8.06×10^{-4}	1.64×10^{-3}	274.89	0.49
43 #3	1.98×10^{-3}	4.09×10^{-3}	197.03	0.49
Δ*mamP*				
43 #1	6.92×10^{-5}	2.09×10^{-4}	64.10	0.33
43 #2	2.89×10^{-5}	8.40×10^{-5}	52.29	0.34
43 #3	1.94×10^{-5}	5.56×10^{-5}	44.71	0.35
Δ*mamT*				
43 #1	0	3.32×10^{-5}	0	0
43 #2	3.58×10^{-6}	3.85×10^{-5}	0	0.09
43 #3	-	-	-	-